Experimental Thermal and Fluid Science 169 (2025) 111540

Contents lists available at ScienceDirect

Experimental Thermal and Fluid Science

journal homepage: www.elsevier.com/locate/etfs

Flow dynamics in cavitation induced micro pumping

V. Agrež, J. Zevnik, Ž. Lokar, M. Dular, R. Petkovšek *

Faculty of Mechanical Engineering, University of Ljubljana, Ljubljana, Slovenia

ARTICLE INFO

Keywords:
Cavitation
Reverse flow
Micro channel
Micro pumping
Rigid boundary
Counter jet

ABSTRACT

The micro pumping process driven by the laser induced cavitation bubbles is scalable, requires only optical access and does not require mechanical moving parts. We investigate how the positioning of the cavitation bubble affects the flow dynamics through differently sized holes in a transparent boundary mimicking a microchannel. For normalized standoff distance above 0.8 and normalized hole radius of 0.22 a significant flow through a hole was observed while decreasing the standoff distance a focused reverse flow was formed impeding downward pumping flow. The details of reverse flow formation were investigated. It was found that bubbles generated next to larger holes with a normalized radius of 0.66 also produce reverse flow, however without it impeding the flow through the structure, even at small normalized standoff distances. Simulations were found to agree well with experiments and used to further study the pumping behavior. Indentation on the bottom side of the bubble was found to be the driver of the focused reverse flow in simulations and differences were investigated for various hole radii and standoff distances. For larger hole radii, reverse flow was found to be both weaker and failed to block the entire hole width, permitting pumping behavior. To improve the flow in the pumping direction, additional structures were produced on top of the flat plate with holes. It was found that adding the entry structure to the hole mitigated the effect of the focused reverse flow on the pumping action.

1. Introduction

Various pumps are used in microfluidics to move liquid, all with different benefits and drawbacks. In addition to passive mechanisms like surface tension [1], active external pumps or microscale pumps are used [2]. For microscale pumping different mechanisms can be used based on effects like electrowetting, piezoelectric, thermopneumatic, pneumatic etc. [3,4]. Among them, a laser induced cavitation bubble can be also used for pumping, either with continuous wave or pulsed [5]. In addition, an external laser can produce breakdown event near a rigid surface with a hole, which offers a possibility of liquid transfer through the hole [6]. One benefit of this approach is that only optical access to the channel is needed, without mechanical parts inside the channel or connection to outside pumps. Further advantage is, that with fine control of the laser energy, arbitrary micrometer-sized bubble diameters are produced [7]. This flexibility offers a one-size-fits-all pumping system for microfluidics, able to adapt to all channel sizes.

Using laser induced cavitation for microfluidics was successfully demonstrated [8]. Laser induced bubbles with the maximum radius between 40 and 50 μm were used to pump liquid through the 20x20 μm^2 opening. Even smaller 5 μm wide channels were used in [9], with different method of pumping. Whereas in the first example, the dominant effect is the movement of the cavitation bubble which moves the liquid, while in the second example the jet through the hole is dominant in pumping the liquid. The relation between the cavitation bubble nucleation distance from a hole and its movement towards it during the pumping action was investigated in [10]. In most cases, the cavitation pumping is investigated near a hole in a flat boundary. The latter having dimensions much larger than the cavitation bubble. It was shown [11] that the cavitation pumping is also viable for a finite boundary with a hole like a capillary that has an opening diameter similar to the bubble maximum diameter. In addition to demonstrating the process, pumping process was further researched in simulations with experimental validation [12]. It was found that bubble size, hole size, hole length and bubble standoff distance all heavily influence the micropumping process and behavior. Those experiments and simulations primarily researched cavitation bubble interaction with a channel where the same liquid is present on both sides of the channel and inside the channel.

Other studies experimentally [13] and numerically [14,15] investigated how the cavitation bubble interacts with boundary that has a hole filled with air for different normalized standoff distances γ. The normalized standoff distance γ being the distance between bubble

* Corresponding author.
E-mail address: rok.petkovsek@fs.uni-lj.si (R. Petkovšek).

https://doi.org/10.1016/j.expthermflusci.2025.111540
Received 21 March 2025; Received in revised form 26 May 2025; Accepted 3 June 2025
Available online 4 June 2025

nucleation point and surface normalized to the bubble maximum radius. At γ greater than one, a simulation comparison to water filled hole was made. It was found that the bubble was jetting towards the boundary despite the presence of air, as the surrounding structure attracts the bubble, exceeding the repulsion effect of the free boundary.

In most experiments, the bubble pushes the liquid through the hole – the flow is from the side with the bubble towards the other side. Similar to the case of the bubble in vicinity of a solid surface, the bubble moves towards the solid surface with the hole during collapse [10,16,17]. In addition to the normal flow or jet in direction towards the hole, flow in the reverse direction (towards the bubble) is also observed in experiments and simulations [18–20]. We name flow towards the cavitation bubble nucleation spot reverse flow, in order to distinguish from the normal flow – in the case of reverse flow, bubble pulls the liquid towards it. Previously, simulations were used to investigate bubble dynamics near a convex plate with a hole, where the normal and reverse flow were studied [21]. They found that there are four different regions of bubble dynamics, with flows in either direction. In cavitation bubble interaction with flat boundary, a larger flow volume in reverse direction was reported [21]. However, their investigation was limited to γ between 1.1 and 2. For low values of γ, Abboud and Oweis experimentally researched counter-jet formation at lower values of γ with spark generated bubbles [22], as did the group of Khoo [18–20]. Reese et al. found that there is a transition between the downward and reverse jet at γ below one [12].

In the present work we investigate the properties of flow that is initiated by the cavitation bubble collapse near a liquid filled hole in a boundary and how the entrance shape influences its formation. Both the normal and reverse flow are observed and studied; focusing of the reverse flow is observed that can impede the normal flow and in consequence the pumping action. Using a normalized standoff distance and normalized hole diameter to the maximum bubble radius a flow direction during bubble first collapse is plotted. Using normalized parameter values the new measurements are combined together with the existing data in the literature [12,18,19,21–23] that consists of different sized bubbles and hole entrances and allows for the first time to define the regions for normal and reverse flow independently of the scale or used nucleation method (Laser and spark induced breakdown). A dominant reverse flow is found in the region of normalized standoff distance lower than 0.8 and normalized hole radius lower than 0.3. Focusing on this region we investigate how different entrance shapes to the hole affect the flow and in consequence pumping dynamics. In addition to the flat structure, we investigated flows with conically shaped entry, leading to a funnel type of structure, as well as a hemispherically shaped entry. Significant differences between the structures are observed in experiments and explained with further investigation using simulations. It is shown that using shaped entrance enables to have normal flow regardless of the combination of the normalized distance and hole diameter.

2. Material and methods

2.1. Experimental setup

The experimental setup (Fig. 1a) included Kirana 7 M high speed camera operated at 1 Mfps, with Cavilux UHS illumination producing 10 ns illumination pulses for each frame. Pulsed laser source (μJ level pulse energy) produces light induced breakdown in water after focusing through a 40x Nikon CFI APO NIR objective with 0.8 *NA*. With the typical pulse power setting of 24 μJ, the generated bubbles had a 150 μm maximum radius resulting in the first oscillation period of approximately 27 μs in infinite liquid. The standoff distance between the bubble nucleation site (laser focus) and the printed structure with a hole was adjusted by the 3D positioning stage. The main parameters of the bubble and structure are shown in Fig. 1b. The most important parameters of the structure are distance from the bubble center to the top of the structure z_0, structure thickness l_h and hole radius R_h. In all experiments,

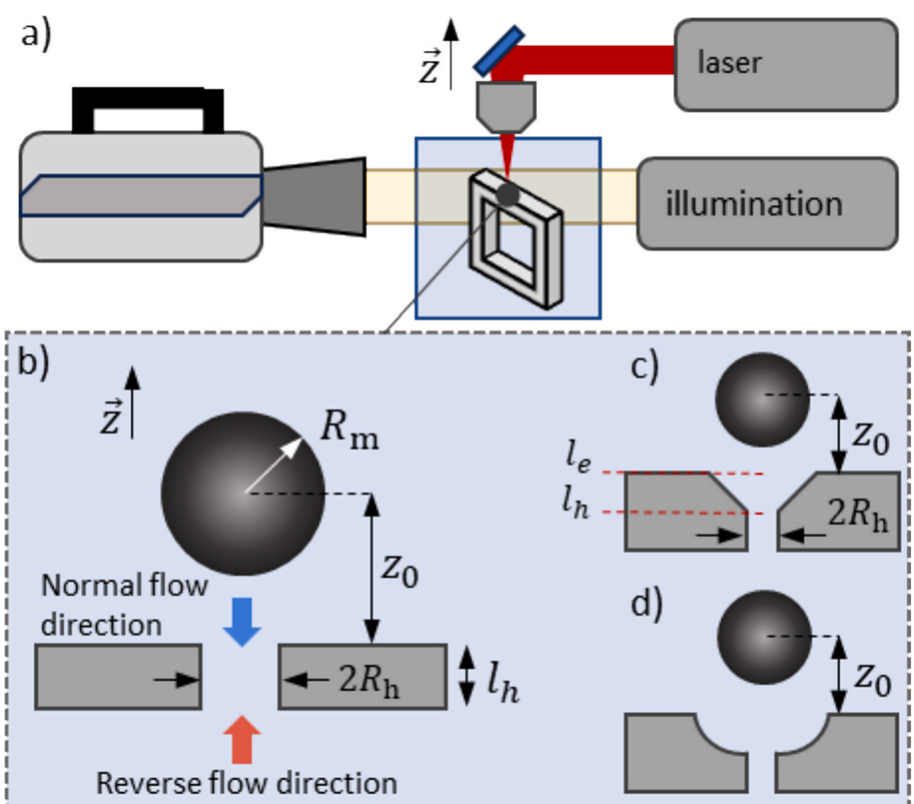

Fig. 1. a) Experimental setup. laser and a high *NA* objective are used to produce cavitation bubbles next to a boundary. b) Illustration of the cavitation bubble next to the structure with the hole. c and d) additional funnel and hemispherical structure, respectively.

bubbles were positioned with the center on the axis through the hole center. This was ensured using another camera parallel to the laser aligned in $\vec{z}$ direction (not shown); plasma was positioned in the center of the hole. In addition to the basic structure with the hole, denoted as "flat", two additional structures were printed on top of the flat structure with the hole to optimize the flow through the structure. These two structures are the same as the "flat" one (that is, R_h and l_h are the same), with addition to the conical funnel (Fig. 1c) or hemispherical (Fig. 1d) addition on the top. The height of both additions was kept the same as well.

It needs to be pointed out that the z_0 is defined as the distance between the bubble and the top plane of the structure. This means that, at the same z_0, distance from the bubble center to the other side of the structure (bottom of the structure) varies between the "flat" and other two structures.

2.2. The microchannel

The microchannel in the experiments was a circular hole with a radius of R_h and length l_h. There are several dimensionless parameters that are defined as the ratio between the structure parameters and the bubble radius R_m:

$$\gamma = \frac{z_0}{R_m} \tag{1}$$

$$\varepsilon = \frac{R_h}{R_m} \tag{2}$$

$$l^* = \frac{l_h}{R_m} \tag{3}$$

Bubble was of a constant size with $R_m = 150$ µm, as were structure thicknesses with $l_h = l_e = 110$ µm. In addition to these parameters, the diameters of the top cross-section of the conical and hemispherical structures are 210 µm and 250 µm, respectively. Other parameters vary in our experiments and simulations, namely z_0 and therefore γ, as well as R_h and thus ϵ.

2.3. Numerical methods

As a part of experimental analysis, optical measurements of the flow were performed. Additionally, numerical simulations were performed to provide further insight into the liquid flow.

Optical measurement of the flow was acquired by processing the images. The first image taken was used as the background and subtracted from all the subsequent images. MATLAB optics flow routine *opticalFlowFarneback* was used to calculate the optical flow. The magnitude of the optical flow below the hole was used to calculate the net flow through the hole. Using pixel size and camera frame rate, flow rate in meters per second was calculated at each point, and from that, the total flow amount through the hole. Circular symmetry was assumed with the axis of symmetry coinciding with the hole center. Because the method in effect tracks the bubbles movements through the frame, it cannot work in case there are no small bubbles produced. In our experiments, small remnant bubbles were always produced during second collapse (collapse of the rebound bubble) and persisted for the duration of the experiment, enabling measurement of velocity at those locations – primarily in the region directly underneath the hole. However, locations where the small bubbles did not arise were unable to be measured – thus, any possible flow before the first rebound could not be imaged. Another thing to note is that the results obtained correspond to bubble velocity, which may be different from liquid velocity given significantly different densities of these phases. However, the velocities measured by optical flow and in numerical simulations agree closely, making the procedure a good proxy for experimental measurement of liquid flow. While some flow was detected for all time scales in the experiments, we are limited by the number of frames the camera captures.

In addition to the described calculation procedure, a simple merging of 3 subsequent images was performed where the image was inverted (so the bubbles became white instead of black). The first image was assigned to the blue color channel, the second image to the green and the third image to the red. This was used for illustrations of the optical flow procedure as it is easier to visualize and serves as an additional indication of correctness of the procedure.

3. Numerical simulations

Numerical simulations were performed to provide insight beyond the resolution of the experiment. We consider compressible, viscous, two-phase flow and employ a Finite volume method-based solver Ansys Fluent [24] along with a Volume of fluid method to capture the interface between phases. The present section includes a general outline of the employed methodology. Further details are given in the Appendix A and our previous work [25].

Two fluid phases are considered – vapor bubble and ambient liquid. In the following sections, quantities and properties specific to each phase are marked by a corresponding subscript $i = v, l$, which denotes the vapor and liquid phase, respectively. Their interface is assumed to remain sharp during the bubble lifetime and the presence of non-condensable gases inside the bubble is neglected. The phase interface is captured by solving the continuity equation for the volume fraction field of the liquid ($i = l$) phase

$$\frac{\partial(\alpha_l \rho_l)}{\partial t} + \nabla\cdot(\alpha_l \rho_l U_l) = S_l \tag{4}$$

Here, α, ρ, and $\boldsymbol{U}$ denote the volume fraction, density, and velocity vector field. Mass transfer in the form of phase change is considered through mass source terms S_l. The volume fraction field of the vapor phase is obtained as $\alpha_v = 1 - \alpha_l$. Following that the volume-averaged fluid properties are determined, which presently holds true for density, dynamic viscosity μ, and thermal conductivity λ. Based on these, a single momentum (Eq. (5) and energy (Eq. (7) equation are solved, which yields the shared velocity $\boldsymbol{U}$ and temperature T fields.

$$\frac{\partial}{\partial t}(\rho U) + \nabla\cdot(\rho U \otimes U) = -\nabla p + \nabla\cdot\tau + b \tag{5}$$

Here p denotes pressure, $\boldsymbol{b}$ body forces, and $\boldsymbol{\tau}$ the viscous stress tensor. The effects of surface tension are included as a body force acting at the vapor–liquid interface. Presently, both phases are considered as Newtonian fluids, and the viscous stress tensor is considered as

$$\tau = \mu\left[\left(\nabla U + (\nabla U)^T\right) - \frac{2}{3}(\nabla\cdot U)I\right] \tag{6}$$

where $\boldsymbol{I}$ denotes the unit tensor.

Energy balance is described by Eq. (7), which includes the effects of thermal conduction and heat transfer due to phase change.

$$\frac{\partial}{\partial t}(\rho E) + \nabla\cdot(U(\rho E + p)) = \nabla\cdot(\lambda\nabla T) + Q \tag{7}$$

Here, E and Q denote the total specific energy and the energy transfer term due to phase change, where the former is considered as a mass averaged variable within a computational cell. The total specific energy of each phase E_i can be expressed by the i-th phase internal energy e_i as

$$E_i = e_i + \frac{|U|^2}{2} \tag{8}$$

Both phases are considered as compressible and are described according to the generalized form of the Noble-Abel Stiffened-Gas equation of state [26,27], such that the vapor phase is effectively considered as a calorically imperfect gas. Additionally, surface tension is modeled according to the Continuum surface stress model [28]. Further details and the values of the material properties considered are given in the

Appendix A.2. Mass transfer in the form of condensation is considered according to the Lee's model [29] as

$$S_v = -S_l = -r_{vl}\alpha_v\rho_v\frac{T_{sat} - T}{T_{sat}}, \text{ when } T < T_{sat}(p) \tag{9}$$

Here, r_{vl} is an empirical coefficient of mass transfer intensity that corresponds to condensation. Term T_{sat} denotes saturation temperature and is presently considered as a function of pressure. The data is taken from the National Institute of Standards and Technology database [30]. The corresponding energy transfer term Q in the energy equation is defined as

$$Q = (h_v - h_l)S_l \tag{10}$$

where the difference between phase enthalpies, h_v and h_l, can be understood as latent heat of vaporization. The consideration of condensation is important as it can significantly affect the bubble collapse and rebound intensity. This is especially prominent in laser-induced bubbles, which can lose more than 90 % of their mass during the first collapse [31]. In the absence of condensation modeling or any other intervention that indirectly accounts for the gradual loss of bubble mass an initially pressurized bubble will yield a weak bubble collapse and large rebounds, which is not characteristic of the presently considered laser-induced bubbles.

A pressure-based variant of the solver is employed, where the Pressure-Implicit with Splitting of Operators pressure–velocity coupling algorithm [32] is used along with first order implicit temporal discretization. Density, momentum, and energy are discretized by the second order upwind scheme, whereas the Pressure Staggering Option scheme [33] is used for pressure discretization. Phase interfaces were captured using a Piecewise linear interface calculation geometric reconstruction scheme [34], which assumes that the interface between two fluids has a linear slope within each computational cell. All cases were evaluated under the assumption of axial symmetry. Orthogonal mesh with a constant resolution of $\Delta x = 0.375$ μm in the region of the bubble was used, which spans 800 computational cells across the maximum bubble diameter. Temporal and spatial resolution were chosen based on the convergence analysis for the case of an unbounded laser-induced bubble given in Table 1. Here, δt and N_{cells} denote the time step increase factor and the number of computational cells, respectively. The finally chosen resolution with $\Delta x = 0.375$ μm and $\delta t = 1.0015$ yields the relative errors for maximum bubble radius R_{max}, minimum bubble radius R_{min}, rebound bubble radius R_{reb}, and peak bubble wall collapse velocity $\frac{dR}{dt}_{min}$ of 0.2 %, 6.1 %, −2.6 %, and −7.4 % in comparison to the resolution independent solutions estimated with the Richardson extrapolation (see bottom row in Table 1). Time step was determined based on the prescribed maximum Courant number of 0.2. Boundary conditions at the end of the computational domain were set to wave non-reflecting pressure outlet with $p_\infty = 10^5$ Pa and $T_\infty = 25$ °C, whereas no-slip walls were considered at the channel boundaries. We assume an initially spherical bubble with radius $R_0 = 7.5$ μm in ambient fluid at rest and even pressure and temperature fields of p_∞ and T_∞. The rate and extent of bubble expansion and collapse is controlled by two parameters, the initial bubble equilibrium radius R_{eq} and condensation intensity factor r_{vl}. Their values were found at $R_{eq} = 62.9$ μm and $r_{vl} = 1.22 \times 10^8$ s^{-1}, according to the three staged trial and error approach (Fig. 2), such that they yield the expansion of an unbounded bubble to the maximum radius $R_{max} = 150$ μm and result in the rebound intensity $R_{reb}/R_{max} = 0.325$ (Fig. 2c). Its value was determined based on the presently obtained experimental results and data from previous research [25]. All simulations were done with the finally chosen spatiotemporal resolution of $\Delta x = 0.375$ μm and $\delta t = 1.0015$. Further modeling details along with the employed values of the material parameters can be found in Appendix A.3 and our previous research [25].

Table 1
Convergence analysis for an unbounded laser-induced bubble.

Δx	δt	N_{cells}	R_{max}	R_{min}	R_{reb}	$\frac{dR}{dt}_{min}$
[μm]	[-]	[10^6]	[μm]	[μm]	[μm]	[m/s]
0.750	1.0030	0.301	150	0.996	47.4	−1360
0.530	1.0021	0.603	150	0.909	48.1	−1450
0.375	1.0015	1.21	150	0.864	48.7	−1510
1/∞	1	∞	150	0.814	50.0	−1630

4. Results and discussion

The image sequence in Fig. 3 shows bubble progression starting from just before the first collapse, 30 μs after breakdown. Results are shown until 60 μs as that shows the main part of pumping dynamics; however, the flow does not cease at that time point, as shown in Fig. 4. Two different γ are shown with distinctly different behavior. For larger γ rebound bubble enters the hole and displaces the liquid, producing strong pumping behavior. On the other hand, smaller γ shows the bubble flattened against the top of the surface. No flow through the hole can be observed.

From the image sequence, starting from breakdown and through all the recorded images, optical flow is calculated as described in section Numerical methods. Maximum velocity of the tracked bubbles, with several accompanying images and the illustration of the optical flow are shown in Fig. 4. For the larger $\gamma = 0.8$, maximum velocity was found to reach nearly 60 m/s for a single 3 μs spike, while smoothed graph of maximum velocity would reach peak of approximately 25 m/s from 40 μs to 60 μs (from Fig. 4c to Fig. 4d). Maximum velocity is always obtained under the hole and near its exit. While the flow is fastest through the hole and at the hole exit, significant fraction of maximum velocity remains few hundred μm below the hole exit, even though the bubbles spread outwards. For longer time scales, beyond 60 μs (Fig. 4d and Fig. 4e), flow slowly decays, however, it does not stop completely. Even at 140 μs after breakdown, zoomed-in optical flow illustration (Fig. 4f), with region marked in Fig. 4e, reveals that the bubbles underneath the hole still move downward. Likewise, small bubbles occasionally present inside the hole also move downward (not shown), which further validates that the flow persists for beyond 100 μs.

On the other hand, flow in the case of the bubble produced at a closer distance with $\gamma = 0.7$ does not exhibit any of these features. As can be seen already in Fig. 3b, the bubble breaks upon collapse, collapsing against the top side of the structure. This results in no net flow through the hole. This is also shown in Fig. 4a where the maximum velocity is low for the whole measurement.

4.1. Flow for different distances between the hole and the bubble

As there was a sharp cutoff between the flow downward and the lack of said flow, this was studied in more detail for different values of γ as well as for two different hole sizes corresponding to different values of ϵ with results shown in Fig. 5.

Significantly different behavior depending on γ is observed for the $\varepsilon = 0.22$ (Fig. 5a) and $\varepsilon = 0.66$ (Fig. 5b). In the case of the smaller hole, there is a significant jump between the different values of γ, which is not observed for the larger hole, where velocity is continuously smaller for smaller values of γ. Causes for the jump with the smaller ε and the lack of it for larger ε is explored in greater detail in the next section 3.2. In addition, maximum velocity for the larger hole is consistently lower in cases of larger flow. This result can be explained by the bubble having the same energy, which is transferred to the liquid. In the case of the larger hole, this energy is spread out over a larger area corresponding to the cross-section of the hole. This results in lower particle and flow velocity, despite higher net flow through the hole.

The change of flow when cavitation bubble interacts with the liquid filled hole was shown in Reese et al. 2022 [12] for fixed normalized hole size of $\varepsilon = 0.2$. This corresponds to the bubble maximum radius of $R_m =$

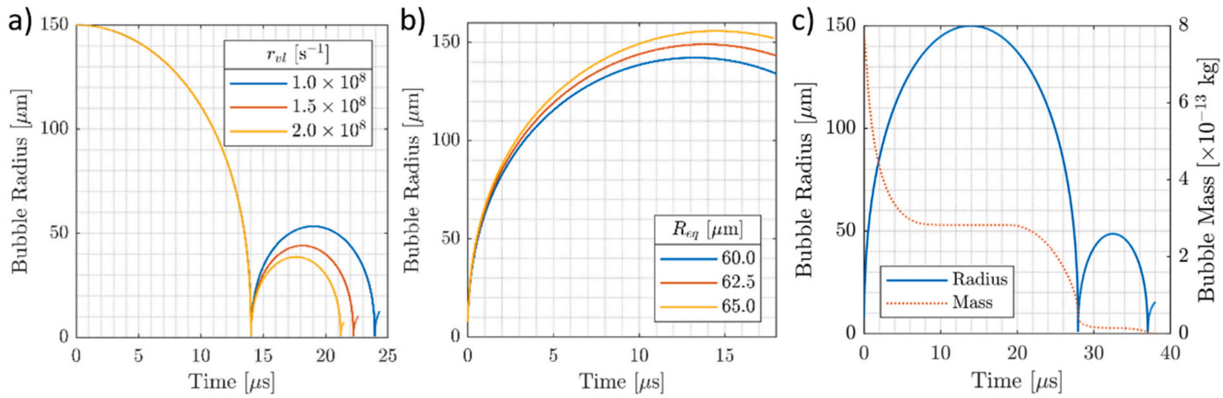

Fig. 2. Preliminary numerical results for unbounded laser-induced bubbles: (a) determination of the condensation coefficient r_{vl}, (b) determination of the initial equilibrium bubble radius R_{eq}, and (c) final results for an unbounded bubble.

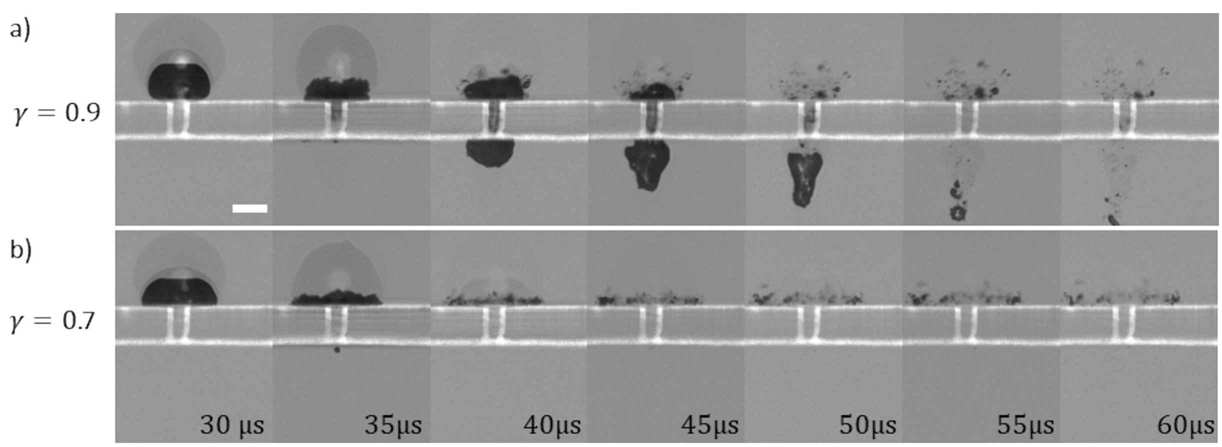

Fig. 3. Image sequence of the bubble collapse near a plate with a cylindrical hole ($\varepsilon = 0.22$) for a) $\gamma = 0.9$ and b) $\gamma = 0.7$. The time after the LIB is denoted on the bottom right of each column and the scale bar is 100 µm.

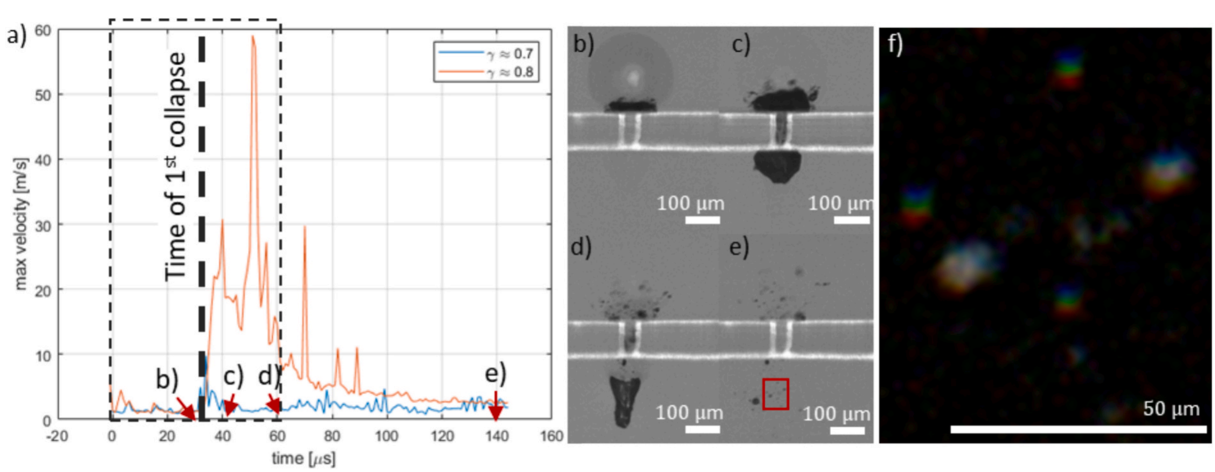

Fig. 4. Flow detection for the cylindrical hole at two standoff distances. a) max velocity with respect to time for two different values of γ. b-e) Images corresponding to different times for $\gamma = 0.8$. f) Optical flow illustration.

460 µm and the hole radius of $R_h = 95$ µm. They measured flow reversal – switch between flow through the hole and formation of focused reverse flow – at approximately $\gamma = 0.7$ which matches the results obtained in this experiment ($\gamma = 0.73$) where approximately three times smaller bubble ($R_m = 150$ µm) and hole ($R_m = 32.5$ µm) were used resulting in $\varepsilon = 0.22$. For comparison, we measured the flow dynamics at the normalized hole length of $l^* = 0.73$ while in the referenced case the normalized length was $l^* = 0.4$.

A combined plot showing both our acquired datapoints as well as the previously existing data on the cavitation bubble induced flow near a hole in a rigid boundary is shown in Fig. 6. All data is for experiments done in water – different viscosities are not considered here, even though they significantly influence pumping dynamics as shown in [12,20]. A flow direction during the bubble first collapse is marked with

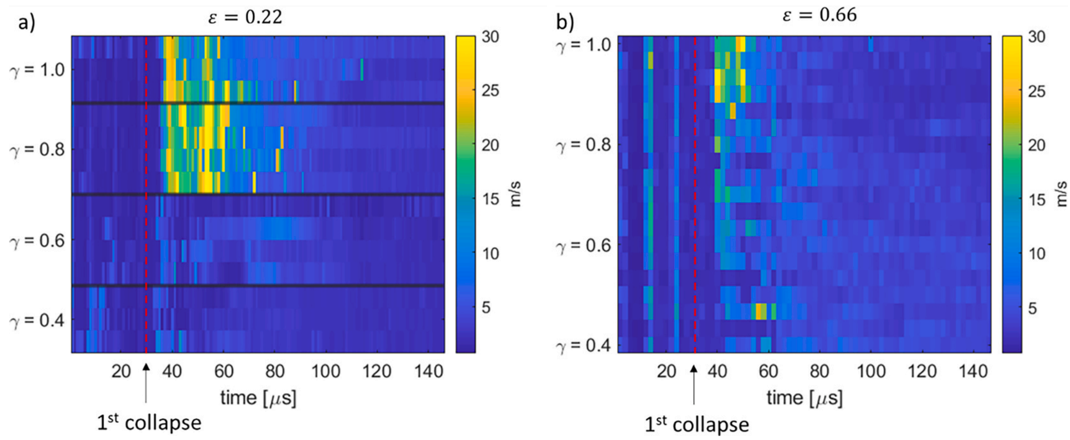

Fig. 5. Flow below the hole measured regarding different normalized standoff distances γ. Subplot a) shows the flows for normalized hole size of $\varepsilon = 0.22$ and b) for $\varepsilon = 0.66$.

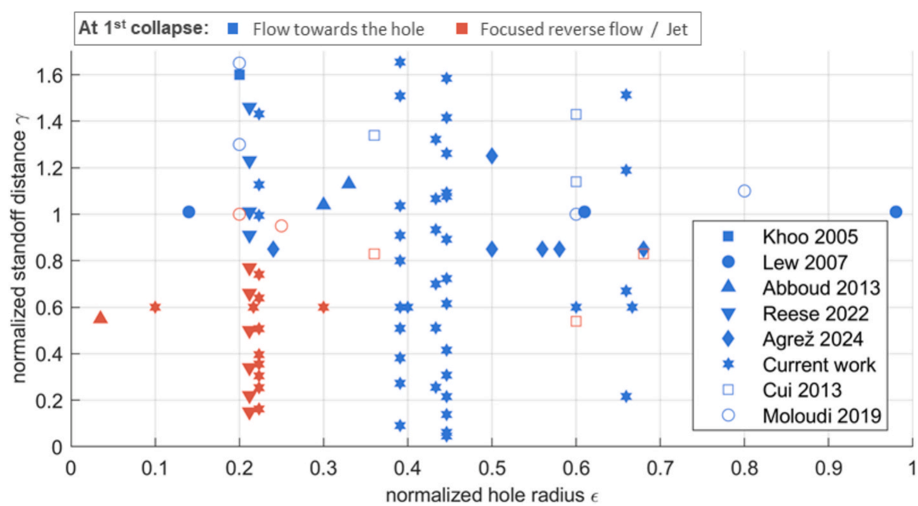

Fig. 6. A flow during the first bubble collapse near a hole in a boundary. The previously published data (different symbols) are presented together with the current work (stars). Solid symbols represent cases when the bubble collapses near a flat solid boundary and the empty symbols the results from the work when boundary was bent.

different colors: blue being towards the hole, red being away from the hole in direction of the bubble. The already published data (different symbols) are presented together with the current work (stars). The data is plotted as normalized standoff distance vs normalized hole radius while for a given experiment different bubble nucleation techniques were used like laser (LIB) or spark induced breakdown. Further, the data plotted is aggregation of different sized cavitation bubbles and holes. Solid symbols represent cases when the bubble collapses near a flat solid boundary: Khoo 2005 [18], Lew 2007 [19], Abboud 2013 [22], Reese 2022 [12] and Agrež 2024 [10], while empty symbols represent the results from the figures in the works when boundary was bent with a radius comparable to the bubble maximum radius: Cui 2013 [23] and Moloudi 2019 [21]. The effect of the concave boundary is seen in offset of the onset of the focused reverse flow to the higher standoff distances and larger normalized hole radius ϵ. The values for cavitation bubble maximum radius, hole diameter and hole length together with the type of the experiment for the above references are shown in Table 2.

Simulations generally use dimensionless quantities – bubble radius, hole radius or plate thickness can be all scaled. Additionally, in experiments the difference between compared largest bubble and the smallest is two orders of magnitude. However, despite absolute differences, derived quantities γ, ε and l^* are all comparable.

Table 2
Cavitation bubble maximum radius, hole diameter and hole length together with the type of the experiment for the selected references.

Work		Type	R_m	R_h	l_h
Khoo 2005	[18]	Simulation	dimensionless	dimensionless	$l^* = 0.4$
Lew 2007	[19]	Spark	4 mm – 5 mm	0.5 mm – 4.5 mm	5 mm
Abboud 2013	[22]	LIB	0.7 mm – 1 mm	0.025 – 0.6 mm	0.2 mm
Reese 2022	[12]	LIB & Simulation	460 µm	95 µm	184 µm
Agrež 2024	[10]	LIB	70 µm – 95 µm	45 µm – 110 µm	110 µm
Cui 2013	[23]	Spark	11.5 mm –13.5 mm	2.2 mm – 14 mm	2 mm
Moloudi 2019	[21]	Simulation	dimensionless	dimensionless	$l^* = 0.5$

4.2. Reverse flow dependence on the hole size

The simulation was used to investigate the formation of the reverse flow during first collapse at the normalized standoff distance $\gamma = 0.6$. Thickness of the boundary was 110 μm and the maximum bubble radius was 150 μm. This standoff distance is right below the optically detected value between strong and negligible flows through the cylindrical hole with the normalized hole size of $\varepsilon = 0.22$. On the other hand, with larger $\varepsilon = 0.60$, there is no experimentally observed blocked flow. The velocity field during the cavitation bubble collapse for both cases are shown in Fig. 7.

Simulations reveal that the reverse flow is present for both values of ε. However, there are significant differences between the cases. In the case of ε = 0.22, shown in Fig. 7a, a focused reverse flow is observed that breaks the collapsing bubble, which then collapses to the sides of the hole. This focused reverse flow is observed as a small protrusion seen at 29 μs and marked with an arrow. A weak flow downwards through the hole is observed in the last column, comparable to the flow upward during bubble collapse in the first column, resulting in little to no net flow through the structure. For the larger hole with ε = 0.60, shown in Fig. 7b, reverse flow velocity is significantly lower. The same protrusion does not occur either. However, total volume of the reverse flow through the hole is comparable. Reverse flow also breaks the collapsing bubble; however, the bubble does not collapse to the sides of the hole but propagates through. This results in significant flow through the hole, with both higher flow velocity and especially total flow than in the case with smaller hole. In addition to different effects on pumping, varying ∊ also produces different shape of the reverse flow, which is presented in Fig. 8.

Looking at the evolution of the reverse flow in Fig. 8a-Fig. 8d shows that the reverse flow forms in two parts. The first part of the reverse flow is caused by the curvature of the bottom part of the bubble. This produces a narrow fluid stream so called focused reverse flow for the case with $\varepsilon = 0.22$ due to its large curvature (small radius). The effect starts and is most easily observed in Fig. 8b with very high velocity upward. This flow drags the liquid throughout the whole channel and produces secondary flow through the hole. Secondary flow encompasses the whole hole, as seen in Fig. 8c, while the focused reverse flow is significantly narrower in the center of the hole at the bubble-water interface. A critical point in reverse jet formation is seen in Fig. 8d where the focused flow protrudes more in the bubble than the wide secondary flow. The shape of a bubble cross section at the same time point for larger hole radii are also shown in Fig. 8e-Fig. 8g. In comparison to the case with $\varepsilon = 0.22$ (Fig. 8d), $\varepsilon = 0.4$ and above do not exhibit the protrusion. The curvature of the top part is also different between the cases. Therefore, it is the flow shape which primarily governs how the collapse occurs and whether the reverse flow prevents forward flow through the hole during collapse. Further analysis was conducted for cases where additional structures were fabricated on top of the "flat" structure to see whether it is possible to improve pumping behavior and mitigate reverse flow effects for smaller values of ε.

4.3. Shaped hole entrance

Conical and hemispherical entrance shape were investigated. Both structures are described and illustrated in Fig. 1, with dimensions listed in section 2.2. In the experiments presented in Fig. 9,γ was the same at 0.3 for both structures while the normalized hole size is $\varepsilon = 0.22$.

At the given $\gamma = 0.3$, flow through the flat structure is negligible due to the formation of the focused reverse flow. Meanwhile, as visually shown in Fig. 9, flow through both structures is significant. This is further shown in Fig. 10, where the optical flow method is used to determine maximum flow velocity through the hole.

Conical and hemispherical structures reach a similar maximum flow velocity through the structure and exhibit similar decay of flow through the structure with time. Both parameters are also notably different at the

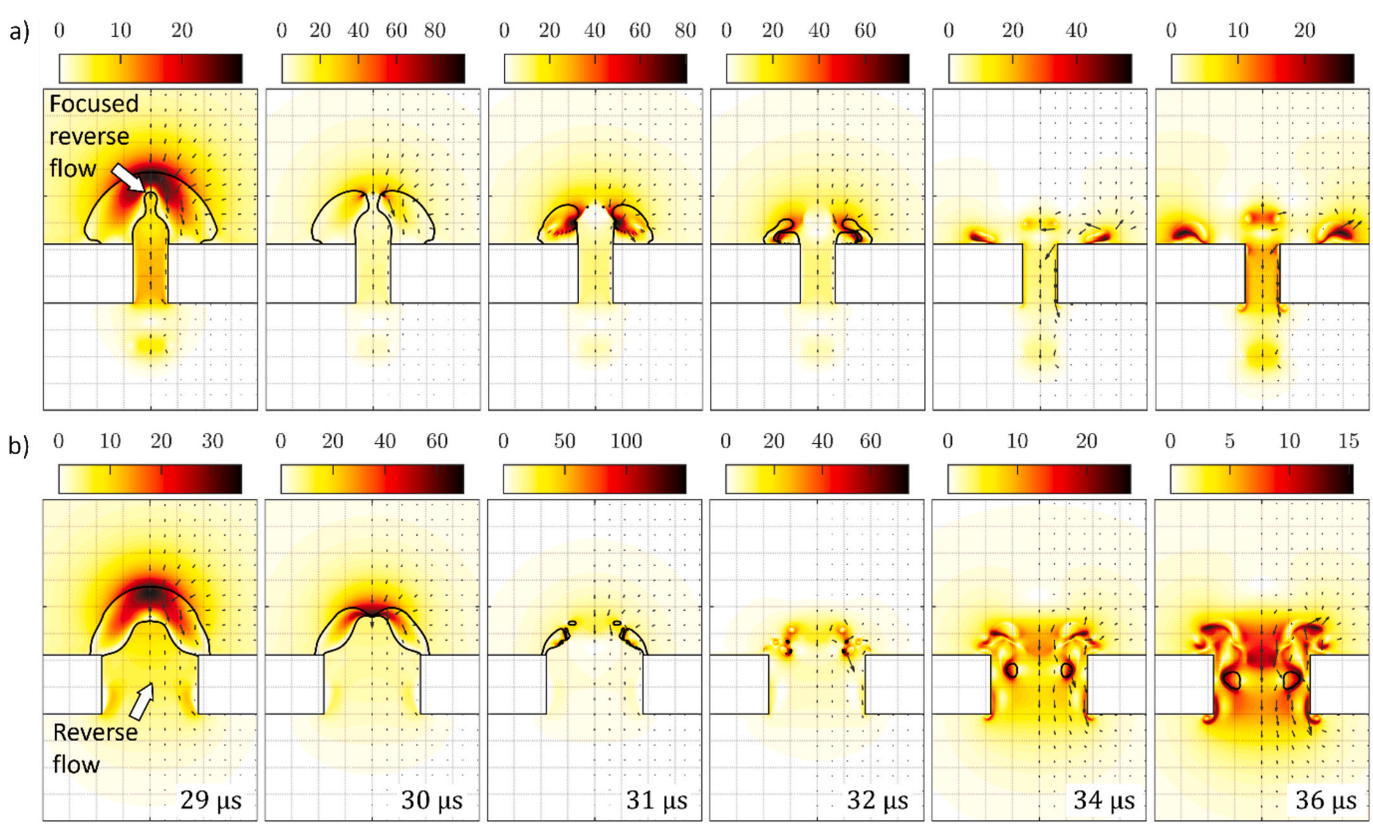

Fig. 7. Reverse flow at normalized standoff distance $\gamma = 0.6$. Shown are velocity field contours (in m/s) along with the bubble shape (black solid line). Grid spacing is 50 μm. Row a) shows the bubble collapse for normalized hole size of $\varepsilon = 0.22$ and b) for $\varepsilon = 0.60$.

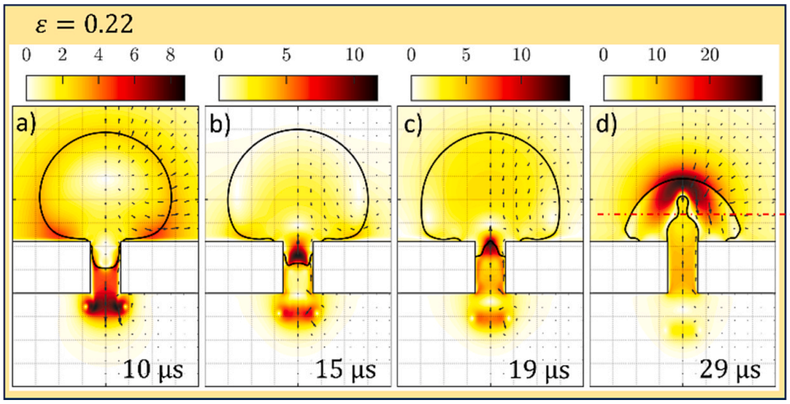

Fig. 8. Reverse flow at normalized standoff distance $\gamma = 0.6$. Shown are velocity field contours (in m/s) along with the bubble shape (black solid line). Grid spacing is 50 µm. a-d show the formation of the reverse flow, while e-g show reverse flow at the same time point for different values of ε. Note that velocity scale is not constant.

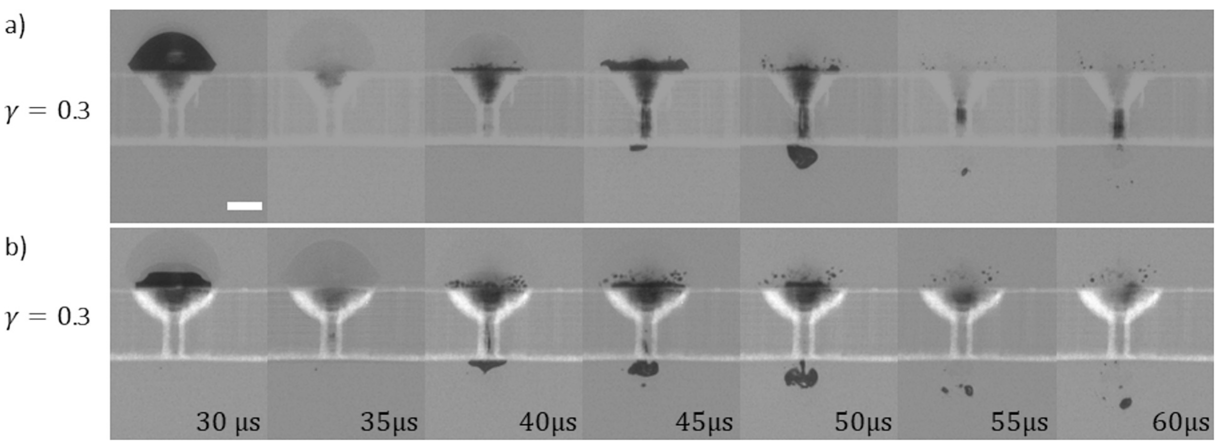

Fig. 9. Image sequence of the bubble collapse near a plate at $\gamma = 0.3$ and $\varepsilon = 0.22$ having a a) conical entrance and b) Hemispherical entrance. The time after the LIB is denoted on the bottom right of each column and the scale bar is 100 µm.

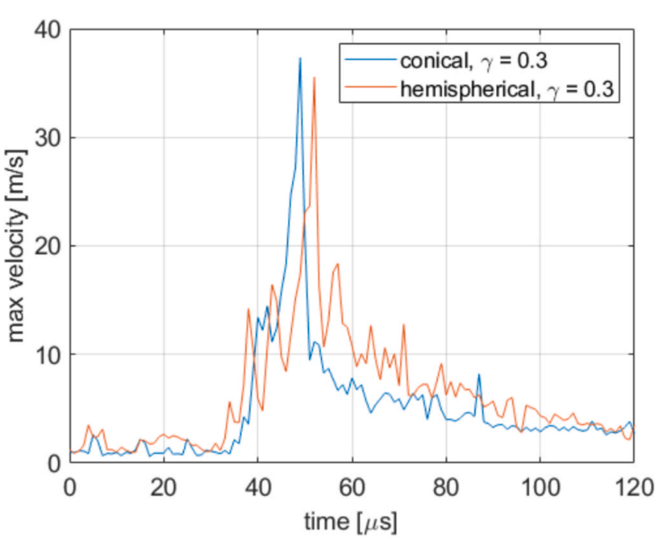

Fig. 10. Maximum velocity of the flow through the structures with shaped entrance at the same normalized standoff distance.

same γ, but similar to the flow through the flat structure at larger γ. Difference between the cases with shaped entry and the flat structure at same γ is primarily caused by the structure shape. However, it also needs to be pointed out that the experiment corresponds to γ of approximately 1.0 for the case of the flat structure with a hole in which case this is a distance where there is a sizeable flow through the channel. Despite the larger cumulative thickness of the structure and the same thickness of the flat part, net flow through the structure is roughly comparable to the flat case for both entrance shapes.

Exploring the differences between the conical and hemispherical structure in more detail, some differences are seen. The first observation is that collapse is slightly faster in case of the hemispherical structure than for the conical structure. Additionally, rebound bubble grows faster in case of the hemispherical structure. Despite these differences, maximum velocity peak of the hemispherical structure occurs later than of the conical one. This is primarily caused by the lifetime of the secondary cavitation bubble. During the rebound bubble collapse, in case of hemispherical structure the bubble splits with some remaining bubbles on the top side and significant flow through the structure. On the other hand, with conical structure the bubble does not propagate through the structure to such a significant extent. These differences and reasons for them were explored in more detail in simulations. First, validation of the simulation and agreement with the experiment is presented in Fig. 11 while simulations of both structures are shown in Fig. 12.

Comparison between the simulation and the experiment shows good agreement with the key features of the bubble shape matching. Additionally, simulations offer insight into local flow velocity throughout the whole bubble dynamics – something which is not observable by the method of optical flow as there are no small bubbles to track. In both experiment and simulation, it is observed that the bubble does not touch

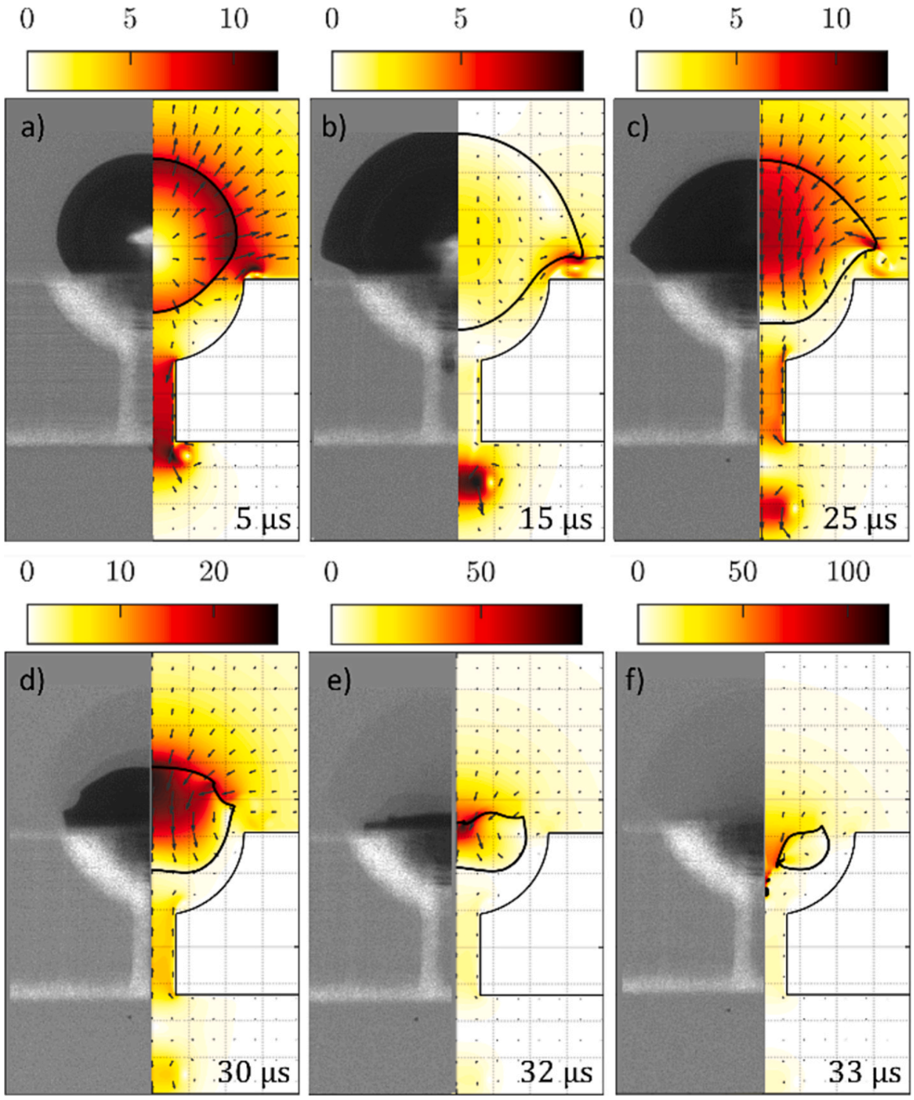

Fig. 11. Comparison between experimental observations (left) and corresponding simulation results (right) for a hemispherical hole entrance at $\gamma = 0.3$. The numerical results show velocity field contours (in m/s) overlaid with the bubble shape (black solid line). Grid spacing is 50 µm.

the walls of the hemispherical cavity. To see whether the bubble fully fills the cavity with different values of γ, a bubble was nucleated inside the hole entrance below the boundary ($\gamma = -0.2$). This γ is small enough that considering just the flat part of the structure, flow would be negligible due to formation of focused reverse flow. Comparison of the bubble behavior and the flow formation in the case of hemispherical and conical hole entrance shape is shown in Fig. 12.

Simulation shows similarities between the bubble behavior in conical and hemispherical cases, leading to the mitigation of the focused reverse flow effect on the pumping action. In both cases a focused reverse flow is produced, as in case of the flat structure. Additionally, thin relatively fast jet towards the channel is formed by the convergent radial flow on the upper half of the bubble (Fig. 12d-Fig. 12g). The latter focuses on the symmetry axis with the majority of the flow in the downwards direction through the channel. In case of the conical structure, the bubble fully fills the opening, as seen in Fig. 12c-Fig. 12f. This leads to delayed collapse phase and formation of stronger reverse flow Fig. 12e that is countered by the perpendicular flow being pulled into the hole by the collapsing bubble observed in Fig. 12e and Fig. 12f. This ultimately causes a jet downward in the pumping direction, as seen in Fig. 12i. On the other hand, for the hemispherical structure, the bubble during its growth does not fill the hemispherical cavity completely. Throughout the bubble growth, liquid remains inside the cavity. This leads to differences during bubble collapse, starting with Fig. 12d. Especially in frames Fig. 12e and Fig. 12f differences are seen between these two structures. The whole collapsing bubble is positioned lower and closer to the center of the hole. In addition to differences in cavitation bubble, liquid flow velocity shows that the focused reverse flow formation is stunted with significantly lower maximum velocity upwards. While those differences would be expected to lead to a stronger flow downward and more efficient pumping mechanism, maximum velocities and flow rates are comparable, as seen in Fig. 12h and Fig. 12i. In summary, both structures allow the continuation of the flow for smaller values of γ, therefore offering improved pumping efficiency compared to the flat case for these distances.

5. Conclusions

This paper shows laser induced cavitation as a promising driver for micro pumping. First, we explore pumping in the case of a cylindrical hole in a flat plate. We found that the cylindrical hole in a flat plate allows for efficient liquid pumping for larger normalized standoff distances between the cavitation bubble and the plate in direction from the bubble through the hole. However, reverse flow formation prevents long-term significant flow through the narrow hole at smaller values of γ. We found the same threshold of $\gamma = 0.7$ for $\varepsilon = 0.2$ in both experi-

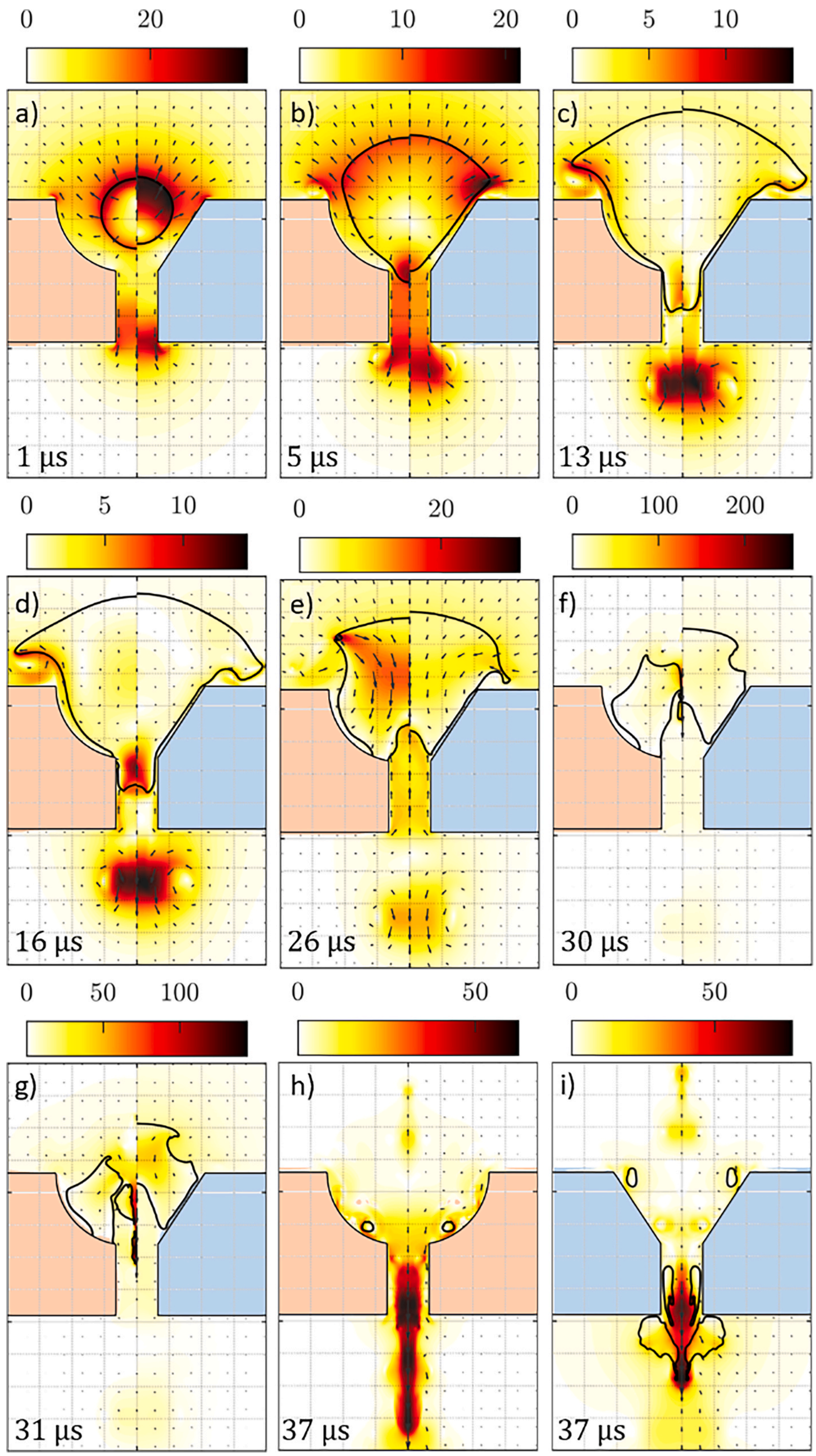

Fig. 12. Comparison between hemispherical (left) and conical (right) hole entrance shape. The bubble is nucleated inside the hole entrance below the boundary ($\gamma = -0.2$). Shown are velocity field contours (in m/s) overlaid with the bubble shape (black solid line). Grid spacing is 50 µm.

ments and simulations, consistent with research of other groups. Detailed study of reverse flow revealed that the reverse flow forms for larger holes as well, but it is not focused and consequently does not prevent downward flow. Thus for larger holes downward flow persisted even at smaller γ.

To increase pumping volume, especially for small normalized standoff distance, additional structures were fabricated on top of the flat plate with the hole. A shaped entrance was used to efficiently funnel the flow into the hole for small and even negative values of γ, in contrast to the flat structure. Both experimental and simulation analysis revealed that dominant downward flow occurs for all values of γ. Simulation results reveal that the primary cause of the downward pumping is the formation of perpendicular flow, which pushes the fluid downward through the hole, despite formation of the reverse flow in the channel.

The practical implementation of cavitation induced microfluidic pumping could be made using a small chamber with optical access for the laser near an output channel. Such a chamber can be integrated into the microfluidic device, for example on each of the mixer input channels. The laser can then be used to simultaneously or alternatively generate cavitation bubbles at the optimized distance in front of the channel and drive or stop the flow accordingly. Further, the formation of focused reverse flow and its interaction with the downward flow is of interest for channel cleaning and can be applied from single hole demonstration to the array of a holes or a membrane.

CRediT authorship contribution statement

V. Agrež: Writing – review & editing, Writing – original draft, Visualization, Methodology, Investigation, Formal analysis, Data curation, Conceptualization. **J. Zevnik:** Writing – review & editing, Writing – original draft, Visualization, Investigation, Funding acquisition, Formal analysis, Data curation, Conceptualization. **Ž. Lokar:** Writing – review & editing, Writing – original draft, Visualization, Methodology, Investigation, Formal analysis, Data curation, Conceptualization. **M. Dular:** Writing – review & editing, Supervision, Investigation, Funding acquisition, Formal analysis, Conceptualization. **R. Petkovšek:** Writing – review & editing, Writing – original draft, Supervision, Investigation, Funding acquisition, Formal analysis, Conceptualization.

Declaration of competing interest

The authors declare that they have no known competing financial interests or personal relationships that could have appeared to influence the work reported in this paper.

Acknowledgements

The authors acknowledge the financial support from the Slovenian Research and Innovation Agency ARIS P2- 0270, P2-0422, Z2-50062, J2-3057, N2-0376 and the interdisciplinary project of the University of Ljubljana: Green Urban Communities of the Future (Phase I: Preparatory Stage).

Appendix

A. Equations of State

Both phases are considered as compressible and are described according to the generalized form of the Noble-Abel Stiffened-Gas equation of state [26,27]. Both liquid (subscript l) and vapor (subscript v) are considered as water.

$$\begin{aligned}
\rho_l(p,T) &= \left[\frac{(\gamma_l-1)C_{vl}T}{p+P_{\infty l}}+b_l\right]^{-1}\\
e_l(p,T) &= \frac{p+\gamma_l P_{\infty l}}{p+P_{\infty i}}C_{vl}T+q_l\\
h_l(p,T) &= \gamma_l C_{vl}T+b_l p+q_l\\
c_l(p,\rho_l) &= \sqrt{\frac{\gamma_l(p+P_{\infty l})}{\rho_l(1-b_l\rho_l)}}
\end{aligned} \tag{A1}$$

Here, h and c denote enthalpy and sound speed, whereas γ, C_v, P_∞, b, and q are the material parameters. A generalized form of the equation of state is employed, which also allows for the consideration of calorically imperfect gases [24]. This is presently true for the vapor phase.

$$\begin{aligned}
\rho_v(p,T) &= \frac{p}{R_v^* T}\\
e_v(T) &= e_{ref_v}+\int_{T_{ref}}^{T} C_{v_v} dT\\
h_v(T) &= h_{ref_v}+\int_{T_{ref}}^{T} C_{p_v} dT\\
c_v(T) &= \sqrt{\gamma_v R_v^* T}
\end{aligned} \tag{A2}$$

Here, R^* and C_p correspond to the specific gas constant and specific heat at constant pressure. The subscript “ref” refers to the value at the reference point (p_{ref}, T_{ref}).

B. Surface tension model

The effects of surface tension at the vapor–liquid interface are considered through a body force term $\boldsymbol{b}$ in the momentum equation according to the Continuum surface stress model [28]:

$$\mathrm{b} = \nabla\cdot\mathrm{S}, \tag{A3}$$

where $\boldsymbol{S}$ is a surface stress tensor defined as

$$\mathrm{S} = \sigma_l(\mathrm{I} - \mathrm{n}\otimes\mathrm{n})|\nabla\alpha_l|. \tag{A4}$$

Here, σ_l denotes the surface tension and $\boldsymbol{n}$ the vapor–liquid interface normal. The latter is obtained as

$$\mathrm{n} = \frac{\nabla\alpha_l}{|\nabla\alpha_l|}. \tag{A5}$$

C. Material parameters

The values of material parameters considered rounded to the first three significant digits are given in Table 3. The remaining material parameters for vapor phase are obtained from the relations in Eq.A6 [27,35]. The employed values of parameters $a_{j,k}$ for calculation of C_{p_v} are taken from [35].

$$\begin{aligned}
&R_v^* = \frac{R_{gas}}{M_v}\\
&C_{p_v} = \begin{cases} R_v^*\sum_{k=-2}^{4} a_{1,k}T^k, & 200\,\mathrm{K} \le T \le 1000\,\mathrm{K} \\ R_v^*\sum_{k=-2}^{4} a_{2,k}T^k, & 1000\,\mathrm{K} < T \le 6000\,\mathrm{K} \end{cases}\\
&C_{vv} = C_{p_v} - R_v^*\\
&\gamma_v = \frac{C_{p_v}}{C_{vv}}\\
&e_{ref_i} = h_{ref_i} - R_i^* T_{ref}
\end{aligned} \tag{A6}$$

Table 3
Values of material parameters considered [36,37].

Parameter (unit)	Value
R_{gas} $\left[\mathrm{J\,kmol^{-1}\,K^{-1}}\right]$	8.31×10^3
p_{ref} [Pa]	3.17×10^3
T_{ref} [K]	298
Vapor phase	
μ_v [Pa s]	9.70×10^{-6}
λ_v $\left[\mathrm{W\,m^{-1}\,K^{-1}}\right]$	1.84×10^{-2}
M_v $\left[\mathrm{kg\,kmol^{-1}}\right]$	18.0
h_{ref_v} $\left[\mathrm{J\,kg^{-1}}\right]$	2.55×10^6
C_{vv} $\left[\mathrm{J\,kg^{-1}\,K^{-1}}\right]$	$f(T)$
Liquid phase	
μ_l [Pa s]	8.90×10^{-4}
λ_l $\left[\mathrm{W\,m^{-1}\,K^{-1}}\right]$	6.07×10^{-1}
σ_l $\left[\mathrm{N\,m^{-1}}\right]$	7.20×10^{-2}
γ_l [−]	1.19
C_{vl} $\left[\mathrm{J\,kg^{-1}K^{-1}}\right]$	3.61×10^3
$P_{\infty l}$ [Pa]	6.22×10^8
b_l $\left[\mathrm{m^3\,kg^{-1}}\right]$	6.72×10^{-4}
q_l $\left[\mathrm{J\,kg^{-1}}\right]$	-1.18×10^6

Data availability

Data will be made available on request.

References

[1] R. Shabani, H.J. Cho, Active surface tension driven micropump using droplet/meniscus pressure gradient, Sens. Actuators B 180 (2013) 114–121, https://doi.org/10.1016/j.snb.2012.05.058.
[2] D.J. Laser, J.G. Santiago, A review of micropumps, J. Micromech. Microeng. 14 (2004) R35–R64, https://doi.org/10.1088/0960-1317/14/6/R01.
[3] B. Parsi, J. Augenstein, R.D. Maynes, N.B. Crane, A low-cost electrowetting on dielectric semi-continuous pump for application to microfluidic reconfigurable devices, Exp. Therm Fluid Sci. 155 (2024) 111183, https://doi.org/10.1016/j.expthermflusci.2024.111183.
[4] W. Krutzsch, P. Cooper, Introduction: classification and selection of pumps, Pump Handbook (2001).
[5] J.J. Schoppink, J. Krizek, C. Moser, D. Fernandez Rivas, Cavitation induced by pulsed and continuous-wave fiber lasers in confinement, Exp. Therm Fluid Sci. 146 (2023) 110926, https://doi.org/10.1016/j.expthermflusci.2023.110926.
[6] S.R.G. Avila, C. Song, C.-D. Ohl, Fast transient microjets induced by hemispherical cavitation bubbles, J. Fluid Mech. 767 (2015) 31–51, https://doi.org/10.1017/jfm.2015.33.
[7] V. Agrež, J. Mur, J. Petelin, R. Petkovšek, Near threshold nucleation and growth of cavitation bubbles generated with a picosecond laser, Ultrason. Sonochem. 92 (2023) 106243, https://doi.org/10.1016/j.ultsonch.2022.106243.
[8] R. Dijkink, C.-D. Ohl, Laser-induced cavitation based micropump, Lab Chip 8 (2008) 1676–1681, https://doi.org/10.1039/B806912C.

[9] K. Cao, Y. Liu, S. Qu, Quantitative microfluidic delivery based on an optical breakdown-driven micro-pump for the fabrication of fiber functional devices, Opt. Express OE 25 (2017) 23690–23698, https://doi.org/10.1364/OE.25.023690.
[10] V. Agrež, Ž. Lokar, R. Petkovšek, Laser induced microbubbles as an alternative driver for liquid pumping, Opt. Laser Technol. 177 (2024) 111235, https://doi.org/10.1016/j.optlastec.2024.111235.
[11] Z. Heidary, Y. Fan, A. Mojra, C.D. Ohl, Robust cavitation-based pumping into a capillary, Phys. Fluids 36 (2024) 123335, https://doi.org/10.1063/5.0238826.
[12] H. Reese, R. Schädel, F. Reuter, C.-D. Ohl, Microscopic pumping of viscous liquids with single cavitation bubbles, J. Fluid Mech. 944 (2022) A17, https://doi.org/10.1017/jfm.2022.480.
[13] Y. Sun, Z. Yao, H. Wen, Q. Zhong, F. Wang, Cavitation bubble collapse in a vicinity of a rigid wall with a gas entrapping hole, Phys. Fluids 34 (2022) 073314, https://doi.org/10.1063/5.0096986.
[14] T.-N. Duy, V.-T. Nguyen, T.-H. Phan, Q.-T. Nguyen, S.-H. Park, W.-G. Park, Numerical study of bubble dynamics near a solid wall with a gas-entrapping hole, Ocean Eng. 285 (2023) 115344, https://doi.org/10.1016/j.oceaneng.2023.115344.
[15] J. Yin, Y. Zhang, X. Qi, L. Tian, D. Gong, M. Ma, Numerical investigation of the cavitation bubble near the solid wall with a gas-entrapping hole based on a fully compressible three-phase model, Ultrason. Sonochem. 98 (2023) 106531, https://doi.org/10.1016/j.ultsonch.2023.106531.
[16] T. Trummler, S.J. Schmidt, N.A. Adams, Effect of stand-off distance and spatial resolution on the pressure impact of near-wall vapor bubble collapses, Int. J. Multiph. Flow 141 (2021) 103618, https://doi.org/10.1016/j.ijmultiphaseflow.2021.103618.
[17] J.R. Blake, D.M. Leppinen, Q. Wang, Cavitation and bubble dynamics: the Kelvin impulse and its applications, Interface Focus 5 (2015), https://doi.org/10.1098/rsfs.2015.0017.
[18] B.C. Khoo, E. Klaseboer, K.C. Hung, A collapsing bubble-induced micro-pump using the jetting effect, Sens. Actuators, A 118 (2005) 152–161, https://doi.org/10.1016/j.sna.2004.08.008.
[19] K.S.F. Lew, E. Klaseboer, B.C. Khoo, A collapsing bubble-induced micropump: An experimental study, Sens. Actuators, A 133 (2007) 161–172, https://doi.org/10.1016/j.sna.2006.03.023.
[20] B. Karri, K.S. Pillai, E. Klaseboer, S.-W. Ohl, B.C. Khoo, Collapsing bubble induced pumping in a viscous fluid, Sens. Actuators, A 169 (2011) 151–163, https://doi.org/10.1016/j.sna.2011.04.015.
[21] G. Moloudi, A. Dadvand, M. Dawoodian, N. Saleki-Haselghoubi, Oscillation of a transient bubble near an aperture made in a convex rigid plate, Eng. Anal. Bound. Elem. 103 (2019) 51–65, https://doi.org/10.1016/j.enganabound.2019.03.005.
[22] J.E. Abboud, G.F. Oweis, The microjetting behavior from single laser-induced bubbles generated above a solid boundary with a through hole, Exp Fluids 54 (2013) 1438, https://doi.org/10.1007/s00348-012-1438-6.
[23] P. Cui, A. Zhang, S. Wang, Q. Wang, Experimental investigation of bubble dynamics near the bilge with a circular opening, Appl. Ocean Res. 41 (2013) 65–75, https://doi.org/10.1016/j.apor.2013.03.002.
[24] ANSYS® Fluent, Release 22.2, 2022, ANSYS, Inc., 2022.
[25] J. Zevnik, J. Patfoort, J.M. Rosselló, C.-D. Ohl, M. Dular, Dynamics of a cavitation bubble confined in a thin liquid layer at null Kelvin impulse, Phys. Fluids 36 (2024) 063340, https://doi.org/10.1063/5.0209287.
[26] O. Le Métayer, R. Saurel, The Noble-Abel Stiffened-Gas equation of state, Phys. Fluids 28 (2016) 046102, https://doi.org/10.1063/1.4945981.
[27] A. Chiapolino, R. Saurel, Extended Noble–Abel Stiffened-Gas Equation of State for Sub-and-Supercritical Liquid-Gas Systems Far from the Critical Point, Fluids 3 (2018) 48, https://doi.org/10.3390/fluids3030048.
[28] B. Lafaurie, C. Nardone, R. Scardovelli, S. Zaleski, G. Zanetti, Modelling Merging and Fragmentation in Multiphase Flows with SURFER, J. Comput. Phys. 113 (1994) 134–147, https://doi.org/10.1006/jcph.1994.1123.
[29] A Pressure Iteration Scheme for Two-Phase Flow Modeling, in: Computational Methods for Two-Phase Flow and Particle Transport, WORLD SCIENTIFIC, 2013: pp. 61–82. https://doi.org/10.1142/9789814460286_0004.
[30] E.W. Lemmon, I.H. Bell, M.L. Huber, M.O. McLinden, Thermophysical Properties of Fluid Systems, NIST Standard Reference Database Number 69, National Institute of Standards and Technology, Gaithersburg MD, 20899, USA, n.d. https://doi.org/10.18434/T4D303 (accessed July 12, 2022).
[31] I. Akhatov, O. Lindau, A. Topolnikov, R. Mettin, N. Vakhitova, W. Lauterborn, Collapse and rebound of a laser-induced cavitation bubble, Phys. Fluids 13 (2001) 2805–2819, https://doi.org/10.1063/1.1401810.
[32] R.I. Issa, Solution of the implicitly discretised fluid flow equations by operator-splitting, J. Comput. Phys. 62 (1986) 40–65, https://doi.org/10.1016/0021-9991(86)90099-9.
[33] C.-J. Hsu, Numerical Heat Transfer and Fluid Flow, Nucl. Sci. Eng. 78 (1981) 196–197, https://doi.org/10.13182/NSE81-A20112.
[34] D. Youngs, Time-Dependent Multi-material Flow with Large Fluid Distortion, Num. Method Fluid Dyn. (1982) 273–285.
[35] B.J. McBride, M.J. Zehe, S. Gordon, NASA Glenn Coefficients for Calculating Thermodynamic Properties of Individual Species, (2002). https://ntrs.nasa.gov/citations/20020085330 (accessed March 11, 2025).
[36] F. Denner, The Gilmore-NASG model to predict single-bubble cavitation in compressible liquids, Ultrason. Sonochem. 70 (2021) 105307, https://doi.org/10.1016/j.ultsonch.2020.105307.
[37] J. Chandran R, A. Salih, A modified equation of state for water for a wide range of pressure and the concept of water shock tube, Fluid Phase Equilibria 483 (2019) 182–188. https://doi.org/10.1016/j.fluid.2018.11.032.